ChemComm

Check for updates

Enhancing the durability of Au clusters in CO₂ photoreduction *via* encapsulation in Cu-based metal–organic frameworks†

Jun Zhang,[a] Xiaofeng Cui,*[ac] Yu Zhou,[c] Tingting Kong,*[a] Yixin Wang,[a] Xianwen Wei [ID][a] and Yujie Xiong [ID]*[ab]

Here, we report the encapsulation of Au_{25} nanoclusters in a $Cu_3(BTC)_2$ metal–organic framework (Au_{25}@Cu-BTC), which can achieve CO_2 photoreduction for selective CO production in a gas–solid reaction system at low-concentration CO_2 atmospheres (even to 0.1%), with remarkably enhanced durability up to at least 48 h.

Light-driven CO_2 reduction has continuously received attention.[1–3] To this end, various photocatalytic materials have been explored for achieving this promising reaction. Very recently, atomically precise metal nanoclusters (NCs) with highly tunable numbers of atoms have emerged as a new class of catalytic materials.[4–7] In particular, their subnanometer sizes (~1 nm), approaching the de Broglie wavelength, result in discrete electronic structures, which makes their light absorption readily tuned.[8,9] Moreover, the ultrasmall sizes and high conductivity of metal NCs are beneficial for the transfer of photogenerated electrons to their surface.[10–12] These characteristics endow the metal NCs with the capability of working for light-driven catalytic reactions. In practical applications, the light-driven catalysts based on metal nanoclusters still typically suffer from two limitations. First of all, metal nanoclusters more readily aggregate into nanoparticles under heating or light illumination due to their extremely high surface energy, leading to the decay of their specific photochemical properties.[13] In the other limitation, the tightly capped ligands on the metal surface, as well as the lack of catalytically active sites, hinder the photogenerated electrons from participating in surface reactions, limiting the catalytic activity.[6]

To prevent aggregation, metal oxides,[14] polymers[15] and covalent organic frameworks[16] can serve as surface coatings. However, these approaches often involve complicated processes and/or can hardly provide effective active sites. Ideally, a surface coating material should not only improve the stability of metal NCs but also offer catalytically active sites for enhancing their catalytic performance. Metal–organic frameworks (MOFs) are crystalline porous materials that can be prepared under mild conditions, and their abundant metal nodes may work as active sites for targeted catalytic applications.[16,17] For this reason, the encapsulation of nanomaterials in MOFs has been intensively studied in recent years.[18,19] However, it remains a great challenge to accomplish surface coating with MOFs because of the lattice mismatch between the guest materials and the MOFs.[20] The abundant surface functional groups and ultrasmall sizes of metal NCs offer the possibility of packaging them in the cavities of a MOF without affecting the framework. Such promising features would make the MOF material an ideal candidate for encapsulating metal NCs to enhance CO_2 photoreduction performance.

Herein, we report a facile process for encapsulating atomically precise Au_{25}(p-MBA)$_{18}$ (p-MBA = 4-mercaptobenzoic acid) clusters in MOFs to enhance the durability of the catalyst in the selective photoreduction of CO_2 to CO. In our designed scheme, the MOFs are expected to introduce multiple advantages for CO_2 photoreduction, *i.e.*, confining Au NCs to prevent aggregation, offering active sites for CO_2 reduction, and capturing CO_2 to facilitate the conversion process. Inspired by these considerations, $Cu_3(BTC)_2$ (BTC = benzene-1,3,5-tricarboxylate) is selected as the MOF model, as it can provide a framework for CO_2 capture and Cu sites for CO_2 activation as demonstrated by our previous studies.[21,22]

Fig. 1a schematically illustrates the synthetic procedure of $Cu_3(BTC)_2$-encapsulated Au_{25}(p-MBA)$_{18}$ (denoted as Au_{25}@Cu-BTC). Water-soluble Au_{25}(p-MBA)$_{18}$ was synthesized according to the method reported by Chen *et al.*[23] The successful preparation of Au_{25}(p-MBA)$_{18}$ was confirmed by UV-vis absorption spectroscopy and ESI mass spectrum (Fig. S1, ESI†). Of particular note is that we selected Au_{25}(p-MBA)$_{18}$ as the model cluster on account of its good

[a] Anhui Engineering Research Center of Carbon Neutrality, The Key Laboratory of Functional Molecular Solids, Ministry of Education, Anhui Laboratory of Molecular-Based Materials, College of Chemistry and Materials Science, Anhui Normal University, Wuhu, 241002, Anhui, P. R. China.
E-mail: xfcui@ahnu.edu.cn, ktt@ahnu.edu.cn, yjxiong@ustc.edu.cn
[b] School of Chemistry and Materials Science, University of Science and Technology of China, Hefei, 230026, Anhui, P. R. China
[c] School of Chemistry and Chemical Engineering, Anqing Normal University, Anqing, 246011, Anhui, P. R. China

Fig. 1 (a) Schematic illustration of the preparation process of the Au$_{25}$@Cu-BTC composite. (b) HRTEM image, (c) STEM image and corresponding EDS elemental mapping images and (d) EDS spectrum of Au$_{25}$@Cu-BTC.

visible light response and facile synthesis. More importantly, the protected ligand of p-MBA has a similar structure to the BTC ligand of MOFs, and as such, its carboxyl group can directly be coordinated with the Cu nodes, which will facilitate electron transfer from the Au NCs to Cu sites in MOFs.

Unlike harsh synthesis conditions (i.e., solvo/hydrothermal methods), we assembled such a hierarchical composite through a mild one-pot solution-phase method to avoid altering the properties of the Au$_{25}$ NCs. In our synthesis, Cu$_2$O nanoparticles rather than Cu^{2+} ions were used as the Cu precursor for Cu$_3$(BTC)$_2$, as we found that directly adding Cu^{2+} inevitably induced Au NC aggregation. The Cu$_2$O nanoparticles can be etched by the protons of carboxyl to slowly release Cu$^+$ and then oxidized to Cu^{2+} by dissolved oxygen, which will coordinate with the carboxyl of BTC and p-MBA to in situ form the encapsulated Au$_{25}$@Cu-BTC.[22] As displayed in the powder X-ray diffraction (PXRD) pattern (Fig. S2, ESI†), the characteristic peak of Cu$_2$O at 2θ = 36.6° (PDF#05-0667) decreased in intensity by prolonging the etching time. When it proceeded to 29 h, this characteristic peak faded thoroughly while the diffraction pattern is consistent with the simulated Cu$_3$(BTC)$_2$, indicating that Cu$_2$O had been completely converted into Cu$_3$(BTC)$_2$. No characteristic peak of Au NCs was found in the PXRD pattern of the Au$_{25}$@Cu-BTC composite, most likely due to the ultrasmall sizes of the Au NCs.

To investigate the structure, high-resolution transmission electron microscopy (HRTEM) was employed to examine Au$_{25}$@Cu-BTC, as shown in Fig. 1b. Au NCs are clearly observed in the HRTEM image and uniformly dispersed in Cu$_3$(BTC)$_2$ with an average diameter of 1.34 nm (Fig. 1b inset). The size is consistent with that of the pristine Au NCs (Fig. S1b, ESI†), confirming that

the Au NCs were well maintained during encapsulation. Cu$_3$(BTC)$_2$ was reported to have cavities with 1.33 nm size and 3D connected channels with 1.8 nm windows,[24] so ultrasmall Au NCs can be confined in the cavities of Cu$_3$(BTC)$_2$ and/or implanted into their channels, preventing the aggregation of the Au NCs. The formation of Au$_{25}$@Cu-BTC was further verified by scanning transmission electron microscopy (STEM) and corresponding energy-dispersive X-ray spectroscopy (EDS) elemental analysis (Fig. 1c and d). The EDS mapping images illustrate that Cu, Au, C, O and S are uniformly distributed, and the good coincidence relation between Cu and O as well as Au and S further confirms that the hierarchical structure has been successfully constructed. The amount of Au in the Au$_{25}$@Cu-BTC composite is determined to be 11.6 wt% by ICP-AES, and the content of Au NCs in this composite is roughly calculated to be 18.1 wt% based on the molecular formula of Au$_{25}$(p-MBA)$_{18}$.

Upon forming the hierarchical structure, we further investigated the interaction between the embedded Au NCs and the coated Cu$_2$(BTC)$_3$ shell using X-ray photoelectron spectroscopy (XPS) and Fourier transform infrared (FT-IR) spectroscopy. The high-resolution O1s XPS spectra (Fig. S4a, ESI†) reveal that Au NCs, Cu$_3$(BTC)$_2$ and Au$_{25}$@Cu-BTC give the most distinct difference in both the existing forms and chemical shifts. The characteristic peaks around 532.5 eV and 531.7 eV can be assigned to hydroxide (H–C–O bonding) and carbonate (C–O bonding), respectively. H–C–O bonding is dominant in the Au NCs, which can be assigned to the uncoordinated carboxyl groups in p-MBA. When the Au NCs are incorporated into Cu$_3$(BTC)$_2$, C–O bonding becomes dominant in Au$_{25}$@Cu-BTC, which can be attributed to the coordination of carboxyl groups of p-MBA with Cu nodes of Cu$_3$(BTC)$_2$ during in situ coating. This argument is confirmed by the shift of the O 1s (Fig. S4a, ESI†), S 2p (Fig. S4b, ESI†) and Au 4f (Fig. S4c, ESI†) characteristic peaks for Au$_{25}$@Cu-BTC toward higher binding energy compared with the pristine Au NCs. This shift is caused by the coordination of carboxyl groups of Au NCs with Cu^{2+}, reducing the electron densities of the p-MBA ligands. In the meantime, the characteristic peaks of Cu in the Cu LMM spectrum of Au$_{25}$@Cu-BTC shift toward lower binding energy compared to bare Cu$_3$(BTC)$_2$ (Fig. S4d, ESI†), as the electron donation by O in the carboxyl of the Au NCs can increase the electron density of the Cu nodes in Cu$_3$(BTC)$_2$. These results demonstrate that the embedded Au NCs are directly connected with the Cu sites of coated Cu$_3$(BTC)$_2$ through coordination bonds, which is also confirmed by FT-IR (Fig. S3, ESI†), providing a good foundation for charge transfer between Au NCs and Cu$_3$(BTC)$_2$. No new Cu species are found on Au$_{25}$@Cu-BTC (Fig. S4d, ESI† and Fig. S4, ESI†).

Upon acquiring the structural characteristics of Au$_{25}$@Cu-BTC, we further examined its performance for CO$_2$ capture and activation. Cu$_3$(BTC)$_2$ has been well demonstrated to have excellent selective sorption for CO$_2$.[25] The CO$_2$ uptake capacity of Au$_{25}$@Cu-BTC was evaluated by comparing the CO$_2$ sorption isotherms with Cu$_3$(BTC)$_2$ under ambient conditions. As revealed by the adsorption and desorption isotherms (Fig. 2a), the CO$_2$ uptake capacity of Cu$_3$(BTC)$_2$ and Au$_{25}$@Cu-BTC was determined to be 100.63 and 62.17 cm^3 g^{-1}, respectively, based on the total weight. Given that Au NCs are not a characteristic

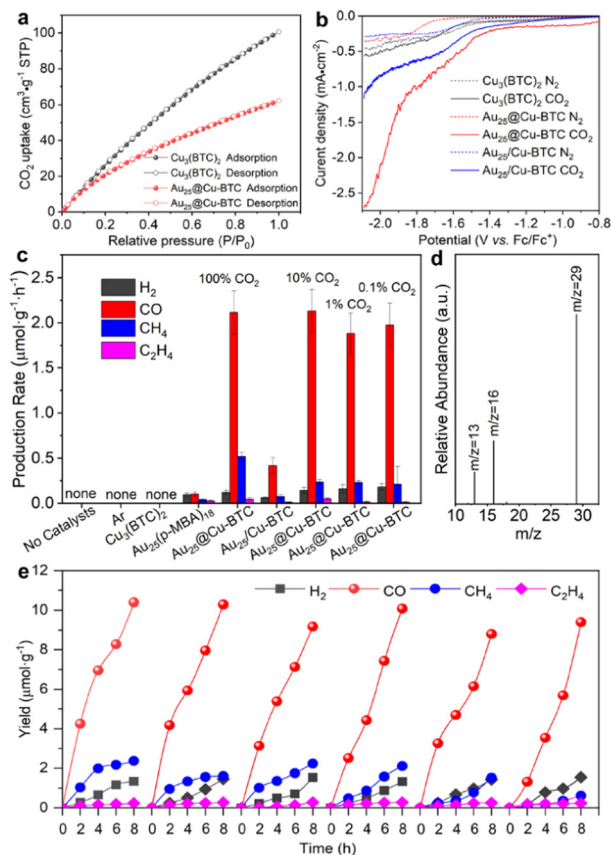**Fig. 2** (a) CO_2 adsorption behavior for Au$_{25}$@Cu-BTC and bare Cu$_3$(BTC)$_2$. (b) LSV curves of pristine Cu$_3$(BTC)$_2$, Au$_{25}$@Cu-BTC and mechanically mixed Au$_{25}$/Cu-BTC in 0.1 M TBAHFP solution saturated with N_2 or CO_2. (c) Average production rates of H_2, CO, CH_4 and C_2H_4 in photoreduction CO_2 by Au$_{25}$@Cu-BTC in the first 2 h under visible-light ($\lambda > 420$ nm) irradiation, in comparison with those by Cu$_3$(BTC)$_2$, Au$_{25}$(p-MBA)$_{18}$, Au$_{25}$/Cu-BTC and other control experiments under the same conditions. All measurements were performed on a gas–solid reactor in the presence of BIH and a trace amount of H_2O. (d) GC–MS analysis of ^{13}CO (m/z = 29) produced over Au$_{25}$@Cu-BTC in light-driven reduction of ^{13}CO$_2$. (e) Light-driven catalytic durability over Au$_{25}$@Cu-BTC. Each cycle takes 8 h.

material for CO_2 adsorption, the CO_2 uptake of the coated Cu$_3$(BTC)$_2$ component is calculated to be approximately 75.91 cm^3 g^{-1}, which is comparable to that of Cu$_3$(BTC)$_2$, indicating that the incorporation of Au NCs does not significantly block the channels of Cu$_3$(BTC)$_2$ for CO_2 capture and mass transfer. This result is confirmed by N_2 sorption measurements (Fig. S5, ESI†) The CO_2 activation ability of the Cu$_3$(BTC)$_2$-based samples was examined by electrochemical linear sweep voltammetry (LSV) measurements in 0.1 M tetrabuty-lammonium hexafluorophosphate (TBAHFP) purged with CO_2 or N_2. As the reference sample, Cu$_3$(BTC)$_2$-loaded Au$_{25}$(p-MBA)$_{18}$ (denoted as Au$_{25}$/Cu-BTC) was prepared *via* a mechanical mixing method. As shown in Fig. 2b, all the samples exhibit higher current density in the CO_2 atmosphere than that in an inert atmosphere, indicating that all of them have the ability to activate CO_2 under a reduction potential. Obviously, the Au$_{25}$@Cu-BTC composite offers the largest increase of current density in the presence of CO_2, which may be attributed to the improvement of electrical conductivity by embedding Au NCs into the framework of Cu$_3$(BTC)$_2$.

Given the excellent performance for CO_2 capture and activation, we are now in a position to examine the performance of Au$_{25}$@ Cu-BTC as a light-driven catalyst for CO_2 reduction. To fully take advantage of the outstanding CO_2 uptake capability, the light-driven catalytic performance was assessed in a gas–solid reactor (Fig. S6, ESI†) under visible-light irradiation using a trace amount (100 μL) of H_2O as a proton source and 1,3-dimethyl-2-phenyl-2, 3-dihydro-1H-benzo[d]imidazole (BIH) as a sacrificial agent to consume photogenerated holes. As shown in Fig. 2c, no reduction products were detected in the absence of catalysts and CO_2, suggesting its strong dependence on both catalysts and CO_2. Consistent with our previous study,[18] pristine Cu$_3$(BTC)$_2$ did not exhibit catalytic activity for CO_2 reduction because it lacks photo-excited electrons for the reduction reaction. Meanwhile, bare Au NCs also presented negligible photoreduction activity and lower selectivity for carbon products (84.1%), which should be due to their lack of active sites for catalyzing reactions.[15] In sharp contrast, when Au NCs were embedded into the Cu$_3$(BTC)$_2$ matrix, the photoreduction activity of Au$_{25}$@Cu-BTC was greatly improved (Fig. 2c and Fig. S7, ESI†). It turned out that the production rate of 2.13 μmol g^{-1} h^{-1} for CO is over 21 times that of bare Au NCs (0.102 μmol g^{-1} h^{-1}), and the selectivity of the carbon products was increased up to 97.6% (Fig. 2c). This enhanced efficiency was achieved through the complementary roles of the two components, with Au NCs serving as a light-harvesting center and Cu$_3$(BTC)$_2$ providing catalytic sites. It has been well verified that Cu sites can suppress the side reaction of hydrogen evolution in photocatalytic and electrocatalytic CO_2 reduction.[21] However, it is difficult to accomplish such an effect by the simply mixed Au$_{25}$/Cu-BTC, which yielded CO at a production rate of only 0.515 μmol g^{-1} h^{-1} (Fig. 2c). This indicates that the connection mode between them is the key for their efficient integration.

Considering the excellent CO_2 capture capability of the Cu$_3$(BTC)$_2$ shell, we evaluated the photoreduction performance of Au$_{25}$@Cu-BTC in a lower concentration CO_2 (10%, 1%, and 0.1%) atmosphere (diluted with argon) under identical reaction conditions. Interestingly, our designed Au$_{25}$@Cu-BTC gives roughly comparable photocatalytic performance in pure and diluted CO_2 atmospheres (Fig. 2c), demonstrating that it has broad application potential in a low-concentration CO_2 atmosphere. To determine the carbon source of the detected CO, isotopic ^{13}CO$_2$ was used as the reactant to carry out the light-driven catalytic reaction under the same conditions, and the product was analysed by gas chromato-graphy–mass spectrometry (GC–MS) (Fig. 2d). The peak appearing at m/z = 29 in MS can be ascribed to ^{13}CO, confirming that CO is indeed produced from the photoreduction of CO_2.

To examine the durability of our catalysts, we performed a test in 6 successive cycles, each of which took 8 h. As shown in Fig. 2e, the catalytic performance of Au$_{25}$@Cu-BTC remained steady for at least 48 h, indicating its excellent durability. HRTEM analysis confirms no distinct size change for the Au NCs confined in the Cu$_3$(BTC)$_2$ matrix (Fig. S8, ESI†). In contrast, bare Au NCs and physically mixed Au$_{25}$/Cu-BTC can hardly maintain their catalytic activity for 2 successive cycles (Fig. S9, ESI†), as the Au NCs tend to be agglomerated into Au nanoparticles (*ca.* 4.5 nm) (Fig. S10, ESI†). These results fully prove that the good durability of
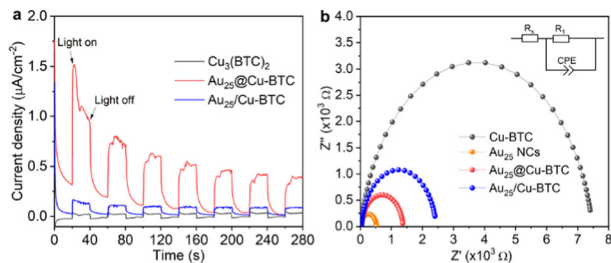
Fig. 3 (a) Photocurrents and (b) Nyquist plots of $Cu_3(BTC)_2$, Au NCs, Au_{25}@Cu-BTC and Au_{25}/Cu-BTC. The inset in (b) is the equivalent circuit for fitting.

Au_{25}@Cu-BTC in CO_2 photoreduction is attributed to the confinement effect of $Cu_3(BTC)_2$ encapsulation.

To gain a deeper understanding on the enhanced performance of Au_{25}@Cu-BTC, we collected the photocurrent response on our catalysts, which has been widely used to reveal the charge separation efficiency. As shown in Fig. 3a, Au_{25}@Cu-BTC exhibits about 4 times higher photocurrent density than Au_{25}/Cu-BTC and 8 times that of bare $Cu_3(BTC)_2$, indicating the superiority of our designed composites for photogenerated charge separation. To find out the reason behind this improvement, Mott–Schottky measurements were applied to examine the charge transfer capability by comparing their resistance. As displayed in Fig. 3b, the charge transfer resistance R_1 drops sharply from 7449 Ω of $Cu_3(BTC)_2$ to 2405 Ω of Au_{25}/Cu-BTC and 1349 Ω of Au_{25}@Cu-BTC, manifesting the smallest internal resistance of Au_{25}@Cu-BTC for its efficient charge transfer. In combining the results of TEM, XPS and FT-IR with the preparation procedure of Au_{25}@Cu-BTC, we can conclude that the efficient charge transfer and separation of Au_{25}@Cu-BTC can be attributed to the following advantages compared with simple mixed Au_{25}/Cu-BTC: (i) the high conductivity Au NCs (Fig. 3b), implanted in the $Cu_3(BTC)_2$ matrix, can improve the overall conductivity for fast transport of photogenerated charges; (ii) the *in situ* implanted Au NCs in $Cu_3(BTC)_2$ are directly connected with Cu sites through chemical bonds between the carboxyl of *p*-MBA and Cu nodes (Fig. S4, ESI†), offering more efficient transfer of photogenerated electrons than the Au_{25}/Cu-BTC through physical contact; (iii) the photogenerated electrons on the embedded Au NCs have shorter migration distances to the Cu sites in the $Cu_3(BTC)_2$ channels than for Au_{25}/Cu-BTC, which can greatly reduce the possibility of charge recombination during travelling to the Cu sites; (iv) more internal Cu sites can be utilized for efficient catalysis in the Au_{25}@Cu-BTC system than in the counterpart of Au_{25}/Cu-BTC.

In summary, we have developed a mild strategy for *in situ* encapsulating ultrasmall Au_{25} nanoclusters in a Cu-based MOF for CO_2 photoreduction, in which the embedded Au NCs produce photoexcited charges while the coated microporous shells capture CO_2 and provide active sites. Remarkably, the light-driven catalytic performance, particularly the durability, was enhanced by our designed Au_{25}@Cu-BTC composite, in stark contrast to bare Au NCs and mechanically mixed Au_{25}/Cu-BTC. The spectroscopic and morphological characterizations have proven that the performance enhancement is attributed to the direct chemical connection of Au NCs with the Cu sites of MOFs promoting charge transfer and the well-matched size between the Au NCs and MOF channels offering a strong confinement effect. This work highlights the importance of ligand and size matching in designing hierarchical photocatalytic materials based on molecular units.

Conflicts of interest

There are no conflicts to declare.

Notes and references

1 X. Wang, M. Sayed, O. Ruzimuradov, J. Zhang, Y. Fan, X. Li, X. Bai and J. Low, *Appl. Mater. Today*, 2022, **29**, 101609.
2 Y. Zhao, G. I. N. Waterhouse, G. Chen, X. Xiong, L. Z. Wu, C. H. Tung and T. Zhang, *Chem. Soc. Rev.*, 2019, **48**, 1972–2010.
3 T. Kong, Y. Jiang and Y. Xiong, *Chem. Soc. Rev.*, 2020, **49**, 6579–6591.
4 Y. Du, H. Sheng, D. Astruc and M. Zhu, *Chem. Rev.*, 2020, **120**, 526–622.
5 X. Kang, Y. Li, M. Zhu and R. Jin, *Chem. Soc. Rev.*, 2020, **49**, 6443–6514.
6 X. Cui, J. Wang, B. Liu, S. Ling, R. Long and Y. Xiong, *J. Am. Chem. Soc.*, 2018, **140**, 16514–16520.
7 M. Y. Gao, H. Bai, X. Cui, S. Liu, S. Ling, T. Kong, B. Bai, C. Hu, Y. Dai, Y. Zhao, L. Zhang, J. Zhang and Y. Xiong, *Angew. Chem., Int. Ed.*, 2022, **61**, e202215540.
8 Q. Yao, X. Yuan, T. Chen, D. T. Leong and J. Xie, *Adv. Mater.*, 2018, **30**, 1802751–1802779.
9 M. A. Abbas, T. Y. Kim, S. U. Lee, Y. S. Kang and J. H. Bang, *J. Am. Chem. Soc.*, 2016, **138**, 390–401.
10 Z. J. Guan, J. J. Li, F. Hu and Q. M. Wang, *Angew. Chem., Int. Ed.*, 2022, **61**, e202209725.
11 R. Jin, G. Li, S. Sharma, Y. Li and X. Du, *Chem. Rev.*, 2021, **121**, 567–648.
12 L. Sementa, G. Barcaro, A. Dass, M. Stener and A. Fortunelli, *Chem. Commun.*, 2015, **51**, 7935–7938.
13 S. Liu and Y. J. Xu, *Sci. Rep.*, 2016, **6**, 22742.
14 B. Weng, K. Q. Lu, Z. Tang, H. M. Chen and Y. J. Xu, *Nat. Commun.*, 2018, **9**, 1543.
15 Y. Deng, Z. Zhang, P. Du, X. Ning, Y. Wang, D. Zhang, J. Liu, S. Zhang and X. Lu, *Angew. Chem., Int. Ed.*, 2020, **59**, 6082–6089.
16 J. X. Gu, C. Y. Sun, X. L. Wang and Z. M. Su, *Chem. Commun.*, 2022, **58**, 10114–10126.
17 M. L. Xu, X. J. Jiang, J. R. Li, F. J. Wang, K. Li and X. Cheng, *ACS Appl. Mater. Interfaces*, 2021, **13**, 56171–56180.
18 Y. Luo, S. Fan, W. Yu, Z. Wu, D. A. Cullen, C. Liang, J. Shi and C. Su, *Adv. Mater.*, 2017, **30**, 1704576.
19 M. L. Xu, M. Lu, G. Y. Qin, X. M. Wu, T. Yu, L. N. Zhang, K. Li, X. Cheng and Y. Q. Lan, *Angew. Chem., Int. Ed.*, 2022, **61**, e202210700.
20 S. Dai, T. Kajiwara, M. Ikeda, I. R. Muñiz, G. Patriarche, A. E. Platero-Prats, A. Vimont, M. Daturi, A. Tissot, Q. Xu and C. Serre, *Angew. Chem., Int. Ed.*, 2022, **61**, e202211848.
21 X. Deng, R. Li, S. Wu, L. Wang, J. Hu, J. Ma, W. Jiang, N. Zhang, X. Zheng, C. Gao, L. Wang, Q. Zhang, J. Zhu and Y. Xiong, *J. Am. Chem. Soc.*, 2019, **141**, 10924–10929.
22 R. Li, J. Hu, M. Deng, H. Wang, X. Wang, Y. Hu, H. L. Jiang, J. Jiang, Q. Zhang, Y. Xie and Y. Xiong, *Adv. Mater.*, 2014, **26**, 4783–4788.
23 T. Chen, V. Fung, Q. Yao, Z. Luo, D. Jiang and J. Xie, *J. Am. Chem. Soc.*, 2018, **140**, 11370–11377.
24 S. S.-Y. Chui, S. M.-F. Los, J. P. H. Charmant, A. G. Open and I. D. Williams, *Science*, 1999, **283**, 1148–1150.
25 Z. Liang, M. Marshall and A. L. Chaffee, *Energy Fuels*, 2009, **23**, 2785–2789.